

# Electron correlations and charge segregation in layered manganese pnictide antiferromagnets showing anomalously large magnetoresistance

N. Janša <sup>1</sup>, K.-K. Huynh <sup>2</sup>, T. Ogasawara,<sup>3</sup> M. Klanjšek,<sup>1</sup> P. Jeglič <sup>1</sup>, P. Carretta,<sup>4</sup> K. Tanigaki,<sup>2,3,5,\*</sup> and D. Arčon <sup>1,6,†</sup>

<sup>1</sup>*Institute Jozef Stefan, Jamova c. 39, 1000 Ljubljana, Slovenia*

<sup>2</sup>*WPI-Advanced Institute for Materials Research (WPI-AIMR), Tohoku University, 1-1-2 Katahira, Aoba, Sendai, Miyagi 980-8577, Japan*

<sup>3</sup>*Department of Physics, Graduate School of Science, Tohoku University, 6-3 Aramaki, Aoba, Miyagi 980-8577, Japan*

<sup>4</sup>*Department of Physics, University of Pavia, Pavia I-27100, Italy*

<sup>5</sup>*Beijing Academy of Quantum Information Sciences, No. 10 Xibeiwang East Rd., Haidian District, Beijing 100193, China*

<sup>6</sup>*Faculty of Mathematics and Physics, University of Ljubljana, Jadranska c. 19, 1000 Ljubljana, Slovenia*



(Received 13 July 2020; revised 8 January 2021; accepted 1 February 2021; published 15 February 2021)

A family of layered manganese-pnictide antiferromagnets  $\text{BaMn}_2\text{Pn}_2$  ( $\text{Pn}$  stands for P, As, Sb, and Bi) has been recently shown to host anomalously large magnetoresistance (MR) with both positive and negative MR components. In search for the microscopic picture of MR in this family, we here report a local-probe  $^{55}\text{Mn}$  nuclear magnetic resonance (NMR) study. The zero-field NMR spectra and the temperature dependence of the spin-lattice relaxation rates are fully consistent with the proposed G-type antiferromagnetic order. However, a close inspection of the  $^{55}\text{Mn}$  NMR spectra reveals a fine structure, which is due to the weakly localized charge carriers. As these carriers localize and segregate in the presence of electron correlations, they also undergo collective spin fluctuations which freeze-out at low temperatures and thus contribute to the  $^{55}\text{Mn}$  spin-lattice relaxation. The characteristic temperatures of the appearance of these additional features in the magnetic response probed by  $^{55}\text{Mn}$  NMR correlate well with the anomalies in the resistivity and anomalously large MR, which hints that the two phenomena are connected.

DOI: [10.1103/PhysRevB.103.064422](https://doi.org/10.1103/PhysRevB.103.064422)

## I. INTRODUCTION

Magnetoresistance (MR), the change of the electrical resistance with a magnetic field, has been over decades reported for a variety of materials. In the vast majority of cases it is a very small effect that rarely exceeds a few percent and is driven by the Lorentz force on the moving charges in two or more band systems [1]. In composite multilayered magnetic metals, the interfacial spins, which respond to the application of magnetic field, can dramatically change the electric transport and MR can reach even up to  $\sim 50\%$ , hence the name giant MR [2]. The so-called colossal MR in the hole-doped perovskite manganites is an even larger effect and can exceed  $10^5\%$  [3,4]. Such an enormous MR effect stems from the switching between the ferromagnetic metal and antiferromagnetic insulating phases. The intertwined charge, spin, orbital and lattice degrees of freedom with a nanoscale mixture of competing electronic phases playing a vital role in enhancing MR make the physics of these strongly correlated systems extremely complex [5].

Here we focus on a family of layered Mn-based compounds,  $\text{BaMn}_2\text{Pn}_2$  [ $\text{Pn} = \text{As, Sb, Bi}$ , Fig. 1(a)], for which electron correlations were also suggested to be important and for which an anomalously large MR with competing positive and negative MR contributions has been recently reported [6]. At low fields a large positive MR up to  $\sim 250\%$  is measured, but then the negative MR contribution prevails already in the

moderate magnetic fields of  $\sim 10$  T where, for instance, the resistivity of  $\text{BaMn}_2\text{Bi}_2$  is dramatically reduced [Fig. 1(b)], yielding MR of  $-98\%$ . Such large and nonmonotonic variation of MR has not yet been observed before and cannot be explained within any of the existing MR models.

$\text{BaMn}_2\text{Pn}_2$  are closely related to the family of high-temperature superconducting iron-pnictides [7]. Specifically,  $\text{BaMn}_2\text{As}_2$  is isostructural to the metallic  $\text{BaFe}_2\text{As}_2$ , but unlike  $\text{BaFe}_2\text{As}_2$ , it is a small gap semiconductor with an antiferromagnetic order of localized Mn moments below the high Néel temperature  $T_N = 625$  K [8–10]. The antiferromagnetic order in  $\text{BaMn}_2\text{As}_2$  has an important difference compared to the spin-density-wave state of  $\text{BaFe}_2\text{As}_2$  [11]: instead of the usual stripe order in the latter compound it shows a G-type antiferromagnetic order, where Mn moments align along the crystallographic  $c$  axis [9]. Very detailed macroscopic and local-probe  $^{55}\text{Mn}$  nuclear magnetic resonance measurements were analyzed utilizing the  $J_1 - J_2$  Heisenberg model for the stacked square lattice, where  $J_1$  and  $J_2$  are the nearest-neighbor and next-nearest-neighbor intraplane exchange interactions and by adding weaker interlayer interactions [10,12,13]. From this, the classical Monte Carlo calculations correctly predict  $T_N$  and the G-type antiferromagnetic order in close agreement with the experiment. Such magnetic order is compliant with a magnetic point group of  $4'/m'mm'$  that is odd under both space inversion and time reversal and allows for the enigmatic higher multipolar spin orders, i.e., hexadecapole order [14].

Density functional calculations for  $\text{BaMn}_2\text{As}_2$  show a substantial hybridization between Mn  $d$  and As  $p$  orbitals in the

\*katsumi.tanigaki.c3@tohoku.ac.jp

†denis.arcon@ijs.si

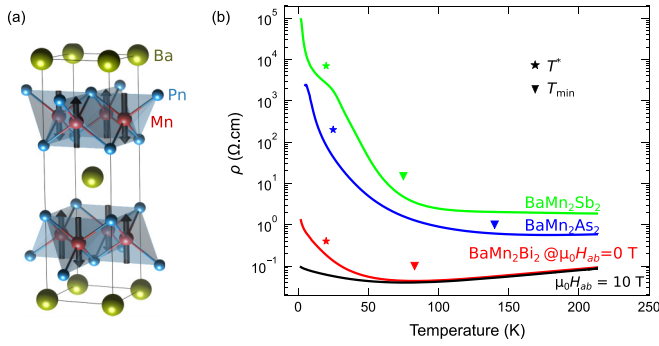


FIG. 1. (a) Crystal structure and the G-type antiferromagnetic order of localized Mn moments (arrows) in the  $\text{BaMn}_2\text{Pn}_2$  ( $\text{Pn} = \text{As}, \text{Sb}, \text{Bi}$ ) family. (b) Temperature dependencies of zero-field resistivity for  $\text{BaMn}_2\text{As}_2$  (blue line),  $\text{BaMn}_2\text{Sb}_2$  (green line), and  $\text{BaMn}_2\text{Bi}_2$  (red line). For comparison, we also show the temperature dependence of the resistivity of  $\text{BaMn}_2\text{Bi}_2$  measured in a magnetic field of 10 T (black line). Triangles and stars mark temperatures  $T_{\min}$  and  $T^*$  (see text for details) for each sample.

valence band, which is separated by a  $\sim 0.05$  eV gap from the narrow conduction band with a predominant Mn  $d$  character [15]. The small bandwidth of the conduction band means that electron correlations may be important for this family. The ordered Mn moments  $\mu \sim 3.8\mu_B$  ( $\mu_B$  is Bohr magneton) are reduced from  $5\mu_B$  anticipated for  $\text{Mn}^{2+}$  due to the effects of hybridization between Mn  $d$  and Pn  $p$  states [15]. Experimentally,  $\text{BaMn}_2\text{As}_2$  is a bad metal at high temperatures [15] due to the presence of the holelike carriers at the top of the valence band [6]. The resistivity [Fig. 1(b)] has a minimum at around  $T_{\min} \sim 140$  K, and then it starts to increase with decreasing temperature because of the weak localization of holelike carriers before showing another anomaly at  $T^* \sim 20$  K [6, 15] of unknown origin. The Bi- and Sb-based compounds show qualitatively the same behavior, albeit  $T_{\min}$  and  $T^*$  do vary with the Pn element [Fig. 1(b)], which may imply that the spin-orbit coupling tuned by the  $d-p$  hybridization plays an important role [6].

With the high-temperature antiferromagnetism, electron correlations, and spin-orbit coupling all present and intertwined,  $\text{BaMn}_2\text{Pn}_2$  may bear some resemblance to the perovskite manganites, which exhibit a colossal magnetoresistance effect. To address the possible origin of the anomalously large MR in  $\text{BaMn}_2\text{Pn}_2$ , we employ the local-probe  $^{55}\text{Mn}$  nuclear magnetic resonance (NMR) technique. The data provide some important insights into the spin states and conduction density of states and single out the importance of electron correlations. Moreover, signatures of localization and of segregation of holelike carriers accompanied with the low-temperature spin freezing are also discussed in terms of strong electron correlations and related to the anomalously large MR in these compounds.

## II. EXPERIMENTAL METHODS

Single crystals of  $\text{BaMn}_2\text{Pn}_2$  antiferromagnets with pnictogen elements As, Sb, and Bi were synthesized using a standard flux method [6]. Specifically,  $\text{BaMn}_2\text{As}_2$  single crystals were grown from a MnAs self-flux, whereas for

the growth of  $\text{BaMn}_2\text{Sb}_2$  and  $\text{BaMn}_2\text{Bi}_2$  single crystals, Sb and Bi metallic fluxes were used, respectively [16]. Single crystals were thoroughly characterized using laboratory x-ray diffraction, energy-dispersive x-ray spectroscopy (EDX), and resistivity measurements [Fig. 1(b)]. The compositions of several crystals were tested by EDX for at least ten sites on each crystal and found no trace of impurities. Examinations by x-ray diffraction also found no trace of impurity phases either, and the widths of the diffraction peaks are narrow. Magnetization measurements observed only conventional antiferromagnetic characteristics matching those published in the literature.  $\text{BaMn}_2\text{Pn}_2$  single crystals show slightly different reactivity when exposed to the air. Although  $\text{BaMn}_2\text{As}_2$  samples are generally quite stable in the air,  $\text{BaMn}_2\text{Bi}_2$  and  $\text{BaMn}_2\text{Sb}_2$  samples display some sensitivity to the atmosphere—typically, the color of these crystals may gradually change after exposure to air for several hours. Therefore during the sample handling special precautions were taken to minimize the sample's exposure to air.

For the measurements of in-plane electrical resistivity  $\rho(T)$ , rectangular samples were cut from the single crystals with freshly cleaved (001) surfaces. Four electrodes were deposited on the  $ab$  plane and along the [100] direction by silver paste for the  $\rho(T)$  measurements. We note that the sample preparation took less than 2 hours to avoid the degradation of the samples in air. Temperature dependencies of  $\rho(T)$  in the magnetic fields of  $\mu_0H = 0$  and 10 T were measured with a Quantum Design physical properties measurement system and a cryostat equipped with an 18-Tesla JASTEC superconducting magnet, respectively. In the case of the  $\text{BaMn}_2\text{Sb}_2$  sample, we define  $T_{\min}$  as the crossing between a linear fit of  $\rho(T)$  in the temperature window from 30 to 50 K and that in the 80–300 K window. Similar method is applied to the other two samples in order to extract the corresponding  $T_{\min}$ .

For the zero-field  $^{55}\text{Mn}$  NMR experiments, single crystals with the approximate sizes of  $1.5 \times 2 \times 0.2$  mm<sup>3</sup> ( $\text{BaMn}_2\text{As}_2$ ) and  $5 \times 7 \times 2$  mm<sup>3</sup> ( $\text{BaMn}_2\text{Sb}_2$  and  $\text{BaMn}_2\text{Bi}_2$ ) were used. The same samples were used also for the  $^{55}\text{Mn}$  NMR experiments conducted in the magnetic field of 9.39 T and with the magnetic field alignment along the crystallographic  $c$  axis. All  $^{55}\text{Mn}$  NMR experiments were conducted in the continuous-flow liquid He cryostat between 2.4 and 300 K using a home-built NMR spectrometer. In the zero-field  $^{55}\text{Mn}$  NMR experiments, a two-pulse solid-echo sequence  $(\beta) - \tau - (\beta) - \tau$  was used with a typical pulse length,  $\tau(\beta) = 5 \mu\text{s}$  (e.g., as optimized for the  $\text{BaMn}_2\text{Bi}_2$  sample), and an interpulse delay of  $\tau = 50 \mu\text{s}$  and the appropriate phase cycling. The pulse length was calibrated on the low-frequency satellite and kept fixed over the entire spectrum. While this can affect the amplitudes of peaks in the quadrupole-split spectrum, it has no effect on the extracted values of the spin-lattice relaxation rates. The complete zero-field wide-line NMR spectra were obtained by integrating NMR signal intensity measured at different excitation frequencies in steps of  $\delta\nu = 50$  kHz. The  $^{55}\text{Mn}$  spin-lattice relaxation rates,  $1/T_1$ , were measured at the center (peak) of the outer satellites with the inversion-recovery technique, typically using 20 increasing time delays  $\tau$  between the inversion pulse and the echo readout sequence. The  $^{55}\text{Mn}$  nuclear magnetization recovery curves were fitted

to the expression

$$M_z(\tau) = M_0[1 - r(0.029 \exp(-\tau/T_1) + 0.214 \exp(-3\tau/T_1) + 0.4 \exp(-6\tau/T_1) + 0.286 \exp(-10\tau/T_1) + 0.071 \exp(-15\tau/T_1))], \quad (1)$$

as appropriate for the nuclear spin  $I = 5/2$  and for the purely magnetic relaxation probed by  $T_1$  measurements on the  $\pm 3/2 \leftrightarrow \pm 5/2$  satellite lines. Here,  $M_0$  is the saturated value of the nuclear magnetization and  $r \sim 1.7$ . At low temperatures, a stretching exponent had to be employed as well. The stretching exponent typically decreased from 1 to  $\sim 0.7$  for temperatures below  $T_{\min}$ .

### III. RESULTS AND DISCUSSION

Temperature dependencies of  $\rho(T)$  for all  $\text{BaMn}_2Pn_2$  samples display qualitatively similar behavior with a metal-to-insulator crossover at  $T_{\min}$  and another anomaly at a lower temperature  $T^*$  [Fig. 1(b)]. For example, in the case of  $\text{BaMn}_2\text{Sb}_2$ ,  $\rho(T)$  is almost temperature-independent from 300 K until around 70 K, below which  $\rho(T)$  clearly upturns into the insulatinglike behavior. The metal-to-insulator crossover is even more pronounced for the  $\text{BaMn}_2\text{Bi}_2$  sample as  $\rho(T)$  exhibits a clear minimum at around 80 K. Previous measurements of the transverse Hall effect show that the conductivity is due to the holelike carriers in the valence band, probably originating from the sample's self-doping [6]. Moreover, these measurements showed that on cooling through  $T_{\min}$  the behavior of the Hall mobility changes from increasing to decreasing (hole carrier number is practically unchanged), which defines  $T_{\min}$  for all three samples. The anomaly in  $\rho(T)$  at  $T_{\min}$  is thus likely due to some localization of such holelike carriers. However, both  $T_{\min}$  and  $T^*$  depend on the  $Pn$  element, as is also indicated in Fig. 1(b). The low-temperature resistivity data is qualitatively well explained by the multi-orbital electronic structure of  $\text{BaMn}_2Pn_2$ , where  $T_{\min}$  marks a crossover from the low-temperature Mott state to the high-temperature metallic state, while  $T^*$  is probably caused by the residual electronic states close to Fermi energy [17].

The self-doping can be triggered by small amounts of impurities. Such small amounts cannot be detected by averaging probes, such as x-ray diffraction and EDX, and thus local-probe NMR measurements have to be employed. The zero-field  $^{55}\text{Mn}$  NMR spectrum of  $\text{BaMn}_2\text{As}_2$  measured at  $T = 5$  K comprises five equidistant peaks [Fig. 2(a)], characteristic for the  $^{55}\text{Mn}$  nuclear spin  $I = 5/2$ . The spectrum is centered at the resonance frequency  $\nu_{ZF} = 241.8$  MHz. The latter corresponds to the internal field  $B_{\text{int}} = 2\pi\nu_{ZF}/\gamma_{\text{Mn}} = 22.9$  T (here  $\gamma_{\text{Mn}}/2\pi = 10.55$  MHz/T is the  $^{55}\text{Mn}$  gyromagnetic ratio), originating from the ordered Mn moment. On the other hand, the splitting between the individual peaks is 2.4 MHz and is entirely due to the nuclear quadrupole interaction. Since the direction of the Mn ordered moments pointing along the crystallographic  $c$  axis coincides with the main eigenaxis of the electric field gradient (EFG) tensor [10], the  $^{55}\text{Mn}$  nuclear quadrupole Hamiltonian simplifies to  $\mathcal{H}_Q = \frac{1}{2}h\nu_Q[I_z^2 - I(I+1)/3]$ , and the splitting between the  $m$  and  $m \pm 1$  spin levels directly measures the quadrupole

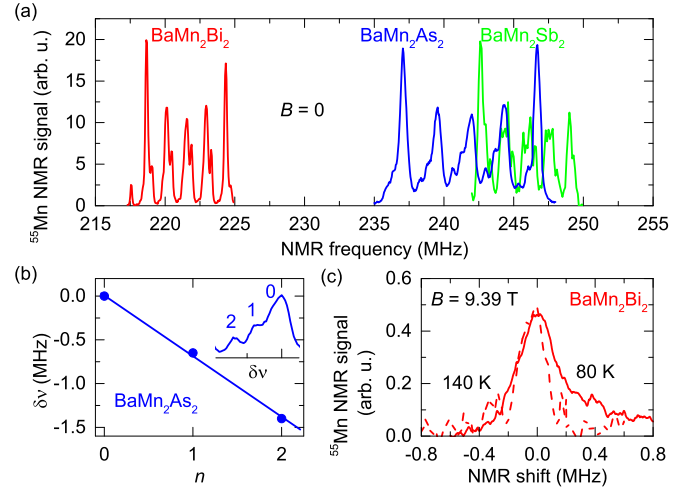


FIG. 2. (a) Comparison of the low-temperature zero-field  $^{55}\text{Mn}$  NMR spectra of  $\text{BaMn}_2\text{As}_2$  (blue line,  $T = 5$  K),  $\text{BaMn}_2\text{Sb}_2$  (green line,  $T = 20$  K), and  $\text{BaMn}_2\text{Bi}_2$  (red line,  $T = 20$  K). (b) The shift  $\delta\nu$  of the additional weaker peaks (inset) with respect to the main peak in  $\text{BaMn}_2\text{As}_2$ . (c) Comparison of  $^{55}\text{Mn}$  NMR spectra of  $\text{BaMn}_2\text{Bi}_2$  measured at 80 K (solid line) and 140 K (dashed line) in the magnetic field of 9.39 T aligned along the crystallographic  $c$  axis. The spectra are shifted to allow for a direct comparison of the fine structure of spectra.

frequency  $\nu_Q$ . All these zero-field  $^{55}\text{Mn}$  NMR line-shape features are in general agreement with the data previously reported in the literature [12]. While the peaks can be found at the same frequencies as in Ref. [12], individual peaks in our zero-field  $^{55}\text{Mn}$  NMR spectra appear broader, thus probably reflecting the presence of a small amount of impurities and related self-doping. Compared to  $\text{BaMn}_2\text{As}_2$ , the low-temperature zero-field  $^{55}\text{Mn}$  NMR spectrum of  $\text{BaMn}_2\text{Sb}_2$  is shifted to slightly higher frequencies, i.e., the center of the spectrum at  $\nu_{ZF} = 246.1$  MHz corresponds to the larger  $B_{\text{int}} = 23.3$  T. On the other hand, the splitting between the individual peaks and thus also  $\nu_Q$  is reduced to 1.7 MHz. Finally, in the case of  $\text{BaMn}_2\text{Bi}_2$ , the spectrum is centered at the lowest frequency at  $\nu_{ZF} = 221.5$  MHz yielding also the smallest  $B_{\text{int}} = 21.0$  T. The peak splitting and the quadrupole frequency now decrease even further down to 1.4 MHz.

The  $^{55}\text{Mn}$  nuclear quadrupole frequency is expressed as  $\nu_Q = \frac{3}{2} \frac{eV_{zz}Q}{2I(2I-1)}$ , where  $Q$  is the quadrupole moment of  $^{55}\text{Mn}$  nucleus and  $V_{zz}$  is the component of the electric field gradient (EFG) tensor  $V_{ij} = \partial^2 V / \partial x_i \partial x_j$ . Since  $\nu_Q$  is proportional to  $V_{zz}$ , it is thus an extremely sensitive probe of the asphericity of the charge distribution around the given nucleus. The observed monotonic decrease of  $\nu_Q$  with the pnictogen element size from 2.4 to 1.4 MHz (Table I) is significant and implies some important charge redistribution within the  $\text{BaMn}_2Pn_2$  family. In the case of iron-based pnictides,  $\nu_Q$  of the pnictogen element is mainly given by the anisotropy of the pnictogen  $p$  orbitals [18]. However, for the Fe nuclei, the picture is more complicated, as there are in general two opposing contributions to EFG: the positive electronic contribution of the valence electrons and the negative nuclear contribution from the nearest atoms surrounding Fe [19]. The valence electronic

TABLE I. Variation of Néel temperature  $T_N$ ,  $^{55}\text{Mn}$  quadrupole frequency  $\nu_Q$ , the low-temperature internal field  $B_{\text{int}}$ , the  $^{55}\text{Mn}$  hyperfine coupling constant  $a_{\text{iso}}$ , and exponent  $\alpha$  for the  $\text{BaMn}_2Pn_2$  ( $Pn = \text{As, Sb, and Bi}$ ) family.

$Pn$	As	Sb	Bi
$T_N$ (K)	625	450	387
$\nu_Q$ (MHz)	2.4	1.7	1.4
$B_{\text{int}}$ (T)	22.9	23.3	21.0
$a_{\text{iso}}$ (T/ $\mu_B$ )	5.84	6.60	5.51
$\alpha$	2.60(6)	2.67(4)	2.51(5)

contribution, which prevails in the case of iron pnictides, can be again split into two parts: the in-plane valence contributions of the  $d_{x^2-y^2}$ ,  $d_{xy}$ ,  $p_x$ , and  $p_y$  orbitals increase  $V_{zz}$ , whereas the out-of-plane  $d_{z^2}$ ,  $d_{zx}$ ,  $d_{yz}$ , and  $p_z$  contributions tend to decrease  $V_{zz}$ . Adopting the same arguments also for the Mn in the studied  $\text{BaMn}_2Pn_2$  family, the monotonic decrease of  $V_{zz}$  (and  $\nu_Q$ ) from  $\text{BaMn}_2\text{As}_2$  to  $\text{BaMn}_2\text{Sb}_2$  to  $\text{BaMn}_2\text{Bi}_2$  samples thus implies the increasing weight of the out-of-plane orbital contributions.

It is interesting to note that the Néel temperature varies within the  $\text{BaMn}_2Pn_2$  family in a similar way as  $\nu_Q$ —it is the highest for the  $\text{BaMn}_2\text{As}_2$  and the lowest for the  $\text{BaMn}_2\text{Bi}_2$  compound. Mean-field theory applied to explain antiferromagnetism in  $\text{BaMn}_2\text{As}_2$  demonstrates that, in addition to the nearest-neighbor  $J_1$ , also the next-nearest-neighbor  $J_2$  intralayer exchange interactions have to be considered [10]. As the latter make the Mn square lattice (Fig. 1) geometrically frustrated, they are primarily responsible for the decrease in  $T_N$ . The increasing weight of the out-of-plane orbital contributions thus appears very efficient in changing the ratio  $J_2/J_1$  and thus also  $T_N$ .

In contrast to  $\nu_Q$ ,  $B_{\text{int}}$  shows more complex  $Pn$  dependence (Table I). Principally,  $B_{\text{int}}$  depends on the size of the Mn sublattice moment and the hyperfine coupling constant  $a_{\text{hf}}$ , i.e.,  $B_{\text{int}} = a_{\text{hf}}\mu$ . The  $a_{\text{hf}}$  is determined by the hybridization between the Mn  $3d$  and the pnictogene  $p$  states. To discuss this point, we use the saturated Mn moments  $\mu_s$  from the literature  $3.88\mu_B/\text{Mn}$  [13],  $3.55\mu_B/\text{Mn}$  [15], and  $3.83\mu_B/\text{Mn}$  [13] to calculate  $a_{\text{hf}} = 5.84 \text{ T}/\mu_B$ ,  $6.60 \text{ T}/\mu_B$ , and  $5.51 \text{ T}/\mu_B$  for the As-, Sb-, and Bi-based compounds, respectively. The hyperfine coupling constant thus varies, unlike  $\nu_Q$ , in a non-monotonic way as the size of the pnictogene element increases. The observed variation in  $a_{\text{hf}}$  somewhat mimics the variation of the resistance among the three samples [Fig. 1(b)]: for example, Sb-based sample is the most insulating and has also the largest isotropic hyperfine constant. Such coincidence may therefore imply that the self-doping due to small amounts of impurities, which introduces the holelike carriers to the top of the valence band and the electronlike carriers to the narrow conduction band, contributes not only to  $\rho(T)$ , but also to the variations in the internal hyperfine field at the  $^{55}\text{Mn}$  site.

Temperature dependencies of the zero-field  $^{55}\text{Mn}$  NMR frequencies,  $\nu(T)$ , for  $\text{BaMn}_2Pn_2$  samples are summarized in Fig. 3. For all three samples,  $\nu(T)$  monotonously decreases with the increasing temperature, which is due to the temperature dependence of the size of the Mn ordered moment

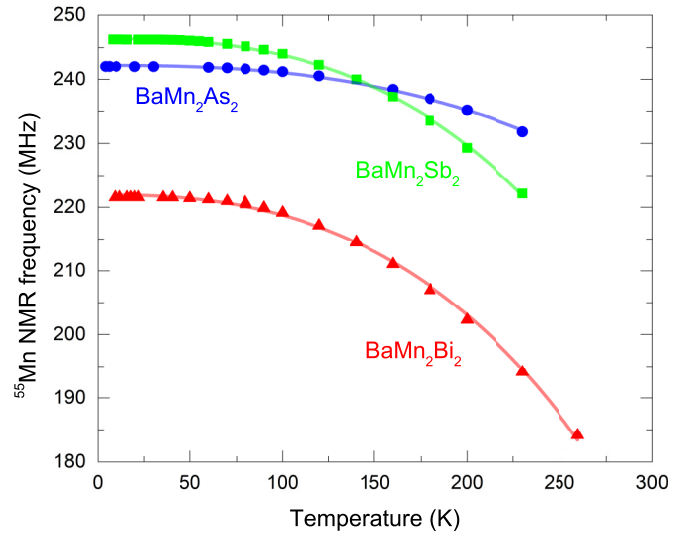


FIG. 3. Temperature dependencies of the zero-field  $^{55}\text{Mn}$  NMR shift for the  $\text{BaMn}_2\text{As}_2$  (blue circles),  $\text{BaMn}_2\text{Sb}_2$  (green squares), and  $\text{BaMn}_2\text{Bi}_2$  (red triangles) compounds. Solid lines are fits with  $\nu(T) = \nu_{ZF}(1 - aT^\alpha)$ .

$\mu$ . The decrease of  $\nu(T)$  with temperature is the strongest for the  $\text{BaMn}_2\text{Bi}_2$  and  $\text{BaMn}_2\text{Sb}_2$  samples, which have lower Néel temperatures of  $T_N = 387$  and  $450$  K, respectively. The decrease is, of course, much more moderate for the  $\text{BaMn}_2\text{As}_2$  sample with the highest  $T_N = 625$  K. For all three samples, the temperature dependence of  $\nu(T)$  can be fitted to  $\nu(T) = \nu_{ZF}(1 - aT^\alpha)$  with an exponent  $\alpha \approx 2.6$  that is close to  $\alpha = 2$  given by the spin-wave theory.

A more careful inspection of the low-temperature zero-field  $^{55}\text{Mn}$  NMR spectra reveals that each quintet of the main peaks is accompanied by another set of five peaks [Fig. 2(a)]. This is most clearly seen for the  $\text{BaMn}_2\text{Bi}_2$  sample where the second weaker set of peaks is shifted to the lower frequencies by 1 MHz, i.e., these particular Mn sites experience by  $\sim 0.1$  T weaker  $B_{\text{int}}$ . Moreover, in  $\text{BaMn}_2\text{As}_2$  even two additional sets of slightly broadened peaks may be recognized. The peak frequencies are in this case equidistantly separated [inset to Fig. 2(b)], and when labeled as peaks  $n = 0-2$ ,  $\delta\nu = \nu_n - \nu_0$  linearly varies with  $n$  [Fig. 2(b)]. Such spectral features suggest the presence of at least two more different local environments for the Mn sites. This is reminiscent of the  $^{55}\text{Mn}$  NMR spectra measured in the  $\text{La}(\text{Ni}_{1-x}\text{Mg}_x)_{0.5}\text{Mn}_{0.5}\text{O}_3$  sample where the additional peaks arise because of the statistical substitution of the magnetic  $\text{Ni}^{2+}$  ions with the nonmagnetic  $\text{Mg}^{2+}$  ions on the nearest-neighbor sites surrounding  $\text{Mn}^{4+}$  site [20]. In the case of  $\text{BaMn}_2Pn_2$ , such  $^{55}\text{Mn}$  local environment differences may be tentatively linked to the presence of self-doping injected charge carriers, which according to the  $\rho(T)$  data localize below  $T_{\text{min}}$ . When these charge carriers localize on the timescale of the NMR experiment, then the separate quintet of  $^{55}\text{Mn}$  NMR peaks may appear for the Mn sites next to the localized charge in the part of the sample with the quenched disorder. The equidistant peak splitting [Fig. 2(b)] allows us to estimate the additional internal field generated by each localized charge to be about  $\approx 0.1$  T, pointing opposite to the field of the main Mn

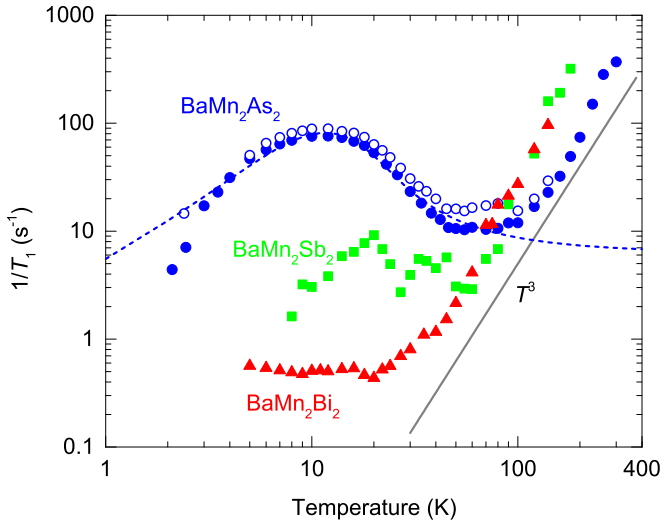


FIG. 4. Temperature dependencies of the zero-field  $^{55}\text{Mn}$  NMR spin-lattice relaxation rates  $1/T_1$  for  $\text{BaMn}_2\text{As}_2$  (blue circles),  $\text{BaMn}_2\text{Sb}_2$  (green squares), and  $\text{BaMn}_2\text{Bi}_2$  (red triangles). All measurements presented by solid symbols are for the most high-frequency peak of the corresponding  $^{55}\text{Mn}$  NMR spectra (Fig. 2). Open blue circles stand for the  $1/T_1$  measured on the low-frequency peak of the  $\text{BaMn}_2\text{As}_2$   $^{55}\text{Mn}$  NMR spectra. Thick gray line is the power-law temperature dependence  $1/T_1 \propto T^{-3}$  predicted for a two-magnon Raman relaxation process [10]. Dashed blue line is a fit of the  $\text{BaMn}_2\text{As}_2$  low-temperature enhancement in  $1/T_1$  to the BPP-type relaxation mechanism using a Gaussian distribution of the activation energies.

antiferromagnetic sublattice. The weakest peak in  $\text{BaMn}_2\text{As}_2$  with  $n = 2$  and with the double internal field thus represents the case with two localized charges next to the given Mn site.

When charge carriers localize below  $T_{\min}$ , they can localize homogeneously over the sample or they can form electronically inhomogeneous phase with the variations in the local density of the charge carriers at the nanoscale, as it is frequently found in the strongly correlated systems [5]. For  $\text{BaMn}_2\text{Pn}_2$  samples it is very difficult to discuss this point by following the temperature evolution of the fine structure of the zero-field  $^{55}\text{Mn}$  NMR spectra across  $T_{\min}$ , because the signal-to-noise ratio significantly degrades at higher temperatures. Nevertheless, it seems that the fine structure of  $^{55}\text{Mn}$  NMR spectra disappears at temperatures above  $T_{\min}$  [Fig. 2(c)], when self-doping charge states ultimately delocalize on the NMR timescale. Moreover,  $\nu(T)$  of the main quintet of peaks, which can be determined very reliably at all temperatures, seems to be insensitive to the drastic changes in the  $\rho(T)$  and the magnetoresistivity at  $T_{\min}$  and  $T^*$ .

Since  $\nu(T)$  measures only the static component of  $B_{\text{int}}$ , we next check the dynamical component of  $B_{\text{int}}$  probed by the  $^{55}\text{Mn}$  spin-lattice relaxation rates  $1/T_1$  (Fig. 4). We stress at this point that the dominant relaxation mechanism must be magnetic, because  $\nu_{\text{ZF}}$  is much larger than the quadrupolar frequency  $\nu_Q$  for all three samples, thus fully justifying the use of Eq. (1). For the  $\text{BaMn}_2\text{As}_2$  single crystal, the temperature dependence of  $1/T_1$  can be divided into two regimes. In the high-temperature regime, which extends from room temperature down to  $T \sim T_{\min}$ ,  $1/T_1$  follows a power-law

dependence  $1/T_1 \propto T^p$  with a power-law exponent  $p \approx 3$  (unconstrained fit yields  $p = 3.4$ ). Such temperature dependence is in full agreement with the published data and can be deep in the antiferromagnetic state explained by the two-magnon Raman relaxation mechanism [10]. For  $T < T_{\min}$ ,  $1/T_1$  starts to deviate from such a power-law dependence and shows a remarkably complex dependence. Namely, on cooling below  $T_{\min}$ ,  $1/T_1$  first starts to increase, and then it reaches a maximum at  $T = 12$  K before decreasing again on further cooling. The observed low-temperature enhancement of  $1/T_1$  cannot be associated with the fluctuations in the quadrupole interactions arising from the phonons or from the charge fluctuations because of the smallness of  $\nu_Q$ . It cannot be due to the presence of randomly localized noninteracting paramagnetic impurities either, as these would lead to a temperature-independent  $1/T_1$  [21,22].

On the other hand, the observed temperature dependence of  $1/T_1$  is qualitatively reminiscent of the so-called Bloembergen-Purcell-Pound (BPP) theory of spin-lattice relaxation, which is based on a local-field fluctuations characterized by a single well-defined thermally activated correlation time,  $\tau_c$  [21]. Since this theory predicts maximum in  $1/T_1$  when  $2\pi\nu\tau_c = 1$ , we can estimate  $\tau_c = 6.5 \times 10^{-10}$  s at  $T = 12$  K. If the BPP-type relaxation mechanism indeed applies, then the maximum in  $1/T_1$  should depend on the Larmor frequency. Therefore we next measured  $1/T_1$  of the lowest-frequency peak of the  $^{55}\text{Mn}$  NMR spectrum. The two datasets of  $1/T_1$  measured at the two different resonance frequencies almost coincide, so it is difficult to judge on the anticipated small temperature shift of the maximum in  $1/T_1$  (Fig. 4). Some distribution in  $\tau_c$  could explain the apparent absence of the frequency dependence of  $1/T_1$ . However, we observe that the values of  $1/T_1$  measured on the low-frequency peak are systematically larger, which is qualitatively consistent with the BPP-type relaxation mechanism as the origin of the low-temperature peak in  $1/T_1$ . In order to address the maximum in  $1/T_1$ , we thus employ a BPP-type relaxation mechanism where the activation energy for the local-field fluctuations has a Gaussian distribution [23] around the average value  $\bar{E}_a/k_B = 33.4$  K and the width of the distribution  $\delta E_a/k_B = 29.1$  K (Fig. 4). For the attempt frequency we get  $\nu_0 = 0.96 \times 10^{11}$  s $^{-1}$ . As  $\bar{E}_a$  is very different from the typical energies for the charge localization (Fig. 1), the low-temperature local-field fluctuations cannot be due to the charge fluctuations. Therefore they must be associated with the low-temperature slowdown of the diffusionlike motion of the hole states in the antiferromagnetic matrix below  $T_{\min}$ , implying the insurgence of low-frequency spin fluctuations [24]. While macroscopic resistivity and local-probe NMR techniques have very different timescales, one would expect to see the maximum in  $1/T_1$  at temperatures lower than  $T_{\min}$  that marks the shallow minimum in the resistivity. This is in the spin-lattice relaxation data quite pronounced for the As-based system and much less for the other two.

Comparing the low-temperature  $1/T_1$  along the  $\text{BaMn}_2\text{Pn}_2$  family, we first notice that the high-temperature magnon-driven relaxation is essentially the same for all three samples. On the other hand, the low-temperature contribution to  $1/T_1$  systematically decreases from As- to Sb- and then finally to a Bi-based sample. Next, in  $\text{BaMn}_2\text{Bi}_2$  the increase in

the low-temperature  $1/T_1$  with decreasing temperature is still observed, although the maximum in  $1/T_1$  is probably shifted to temperatures below  $T = 5$  K due to the very large  $\delta E_a$ . The quality of the  $1/T_1$  data measured on  $\text{BaMn}_2\text{Sb}_2$  is not sufficient to judge whether  $1/T_1$  increases with decreasing temperature at low temperatures or not.

We point out that the low-temperature enhancement of  $1/T_1$  seems to be sample dependent—in the data published in Ref. [12] on the  $\text{BaMn}_2\text{As}_2$  compound the low-temperature contribution to the relaxation is weaker than for the sample reported here. This corroborates our conclusion that it is induced by the presence of impurities that trigger self-doping, i.e., the low-temperature spin fluctuations originate from the hole states at the top of the  $d$ - $p$  valence band or from the electron states in the narrow  $d$  conduction band. As these states according to the resistivity data gradually localize below  $T_{\min}$  [Fig. 1(b)], the increase in  $1/T_1$  with decreasing temperature can be attributed to the growth of their spin fluctuations. In our case, the observed enhancement in  $1/T_1$  is in fact quite substantial—for the  $\text{BaMn}_2\text{As}_2$  sample at the local maximum of  $1/T_1$  at  $T = 12$  K, the value of  $T_1$  is only 10 ms and is comparable to the values of  $T_1$  at ambient temperatures. This indicates that the localized charge carriers cannot be simply treated as noninteracting random spins (or be linked to the presence of impurities randomly incorporated into the structure), but they rather show a cooperativelike phenomena where the typical correlation times of the respective spin fluctuations cross the NMR timescale below  $T_{\min}$ . The comparative magnitude of  $\bar{E}_a$  and  $\delta E_a$  is more consistent with a broad distribution of such spin clusters than with the formation of so-called stripes and may also explain the decrease of the stretching exponent to  $\sim 0.7$  below  $T_{\min}$ . The maximum in  $1/T_1$ , observed for the  $\text{BaMn}_2\text{As}_2$  sample, then suggests a certain type of spin freezing, probably due to the development of static (short-range) spin correlations in the part of the sample where localized charges cluster.

If these samples are close to self-doping, then self-doping can be triggered by even a small amount of impurities (this would explain the characteristic broadening of our  $^{55}\text{Mn}$  NMR spectra compared to those in Ref. [12]). Next, if the self-doping introduces electron states in the  $d$  band and if these states are responsible for such a behavior, then an interesting explanation for the low-temperature magnetism and the magnetoresistance emerges. Namely, electron correlations within the narrow  $d$  band may drive the orbitally selective Mott transition [25] and explain both the increase of  $\rho(T)$  as well as the enhanced antiferromagnetic spin fluctuations below  $T_{\min}$ . In such a case, the magnetic moments associated with these localized  $d$  band states may easily reorient even in the moderate external magnetic fields. If they are coupled to the majority of  $d$ - $p$  valence band moments, then such coupling could also trigger tilting of the Mn sublattice magnetization and may explain the observed anomalously large magnetoresistance response [6]. On the other hand, if the hole states at the top of the  $d$ - $p$  valence band are the ones to be considered, then they can localize below  $T_{\min}$  only through some weak localization

mechanism [26]. In this case the MR is predicted to be negative, because the magnetic field destroys the phase coherence that is essential for producing the interference effects in the weak localization mechanism [27]. In the zero field, electrons tend to doubly occupy the lowest energy states in order to minimize the effect of weak-localization-induced fluctuations. As a result, quenching of the local moments is expected, which is in apparent disagreement with the low-temperature  $1/T_1$  data and the enhanced spin fluctuations observed on the NMR timescale. In order to restore the magnetic moment and spin fluctuations again, some electron correlations have to be considered, which finally opens also a possibility of positive MR contributions [28]. The present data thus suggest that charge localization and segregation due to the electron correlations are important for  $\text{BaMn}_2Pn_2$ , but more theoretical and experimental work is needed in the future in order to discriminate between the two scenarios that link the anomalously large MR and the low-temperature spin dynamics and the related enhancement in  $1/T_1$  in the  $\text{BaMn}_2Pn_2$  family.

#### IV. CONCLUSIONS

In conclusion, we have studied the family of  $\text{BaMn}_2Pn_2$  compounds in which anomalously large MR has been recently discovered. In full agreement with the published data, a zero-field  $^{55}\text{Mn}$  NMR can be consistently explained within the proposed G-type antiferromagnetic order. A close inspection of the spectra, on the other hand, discloses the presence of additional weaker  $^{55}\text{Mn}$  resonances, which mark the Mn sites next to the localized charge carriers. The unexpected low-temperature enhancement in  $1/T_1$  suggests that these localized charge states may phase segregate and exhibit a spin freezing process, which is a fingerprint of electron correlations. As the observed spin phenomena coincide with the anomalies observed in  $\rho(T)$  and evolution of the positive and negative components of MR, it is thus tempting to link the two phenomena.

#### ACKNOWLEDGMENTS

This work was supported by a Grant-in-Aid for Scientific Research on Innovative Areas “J-Physics” (Grant No. 18H04304) and by JSPS KAKENHI (Grants No. 18K13489, No. 18H03883, No. 17H045326, and No. 18H03858). This research was partly made under financial support by the bilateral country research program of JSPS between AIMR, Tohoku University, and Jožef Stefan Institute, Slovenia. This work was also supported by the World Premier International Research Center Initiative (WPI), MEXT, Japan. T.O. is thankful for financial support from the International Joint Graduate Program in Materials Science (GP-MS) of Tohoku University. We acknowledge the High Field Laboratory for Superconducting Materials (HFLSM) at Tohoku University for support during the experiments at high magnetic fields. D.A. acknowledges financial support of the Slovenian Research Agency through Grants No. BI-JP/17-19-004, No. BI-JP/20-22-004, and No. J1-9145.

- [1] J. M. Ziman, *Principles of the Theory of Solids* (Cambridge University Press, Cambridge, England, 1972).
- [2] M. N. Baibich, J. M. Broto, A. Fert, F. N. Van Dau, F. Petroff, P. Etienne, G. Creuzet, A. Friederich, and J. Chazelas, *Phys. Rev. Lett.* **61**, 2472 (1988).
- [3] Y. Tokura, *Rep. Prog. Phys.* **69**, 797 (2006).
- [4] M. B. Salamon and M. Jaime, *Rev. Mod. Phys.* **73**, 583 (2001).
- [5] E. Dagotto, *Science* **309**, 257 (2005).
- [6] K.-K. Huynh, T. Ogasawara, K. Kitahara, Y. Tanabe, S. Y. Matsushita, T. Tahara, T. Kida, M. Hagiwara, D. Arčon, and K. Tanigaki, *Phys. Rev. B* **99**, 195111 (2019).
- [7] Y. Kamihara, T. Watanabe, M. Hirano, and H. Hosono, *J. Am. Chem. Soc.* **130**, 3296 (2008).
- [8] Y. Singh, A. Ellern, and D. Johnston, *Phys. Rev. B* **79**, 094519 (2009).
- [9] Y. Singh, M. A. Green, Q. Huang, A. Kreyssig, R. J. McQueeney, D. C. Johnston, and A. I. Goldman, *Phys. Rev. B* **80**, 100403(R) (2009).
- [10] D. C. Johnston, R. J. McQueeney, B. Lake, A. Honecker, M. E. Zhitomirsky, R. Nath, Y. Furukawa, V. P. Antropov, and Y. Singh, *Phys. Rev. B* **84**, 094445 (2011).
- [11] M. Rotter, M. Tegel, D. Johrendt, I. Schellenberg, W. Hermes, and R. Pöttgen, *Phys. Rev. B* **78**, 020503(R) (2008).
- [12] S. Yeninas, A. Pandey, V. Ogloblichev, K. Mikhalev, D. C. Johnston, and Y. Furukawa, *Phys. Rev. B* **88**, 241111(R) (2013).
- [13] N. S. Sangeetha, V. Smetana, A.-V. Mudring, and D. C. Johnston, *Phys. Rev. B* **97**, 014402 (2018).
- [14] H. Watanabe and Y. Yanase, *Phys. Rev. B* **96**, 064432 (2017).
- [15] J. An, A. S. Sefat, D. J. Singh, and M.-H. Du, *Phys. Rev. B* **79**, 075120 (2009).
- [16] B. Scharov, D. J. Singh, V. O. Garlea, and A. S. Sefat, *Sci. Rep.* **3**, 2154 (2013).
- [17] L. Craco and S. S. Carara, *Phys. Rev. B* **97**, 205114 (2018).
- [18] P. Jeglič, J.-W. G. Bos, A. Zorko, M. Brunelli, K. Koch, H. Rosner, S. Margadonna, and D. Arčon, *Phys. Rev. B* **79**, 094515 (2009).
- [19] M. Alzamora, J. Munevar, E. Baggio-Saitovitch, S. L. Bud'ko, N. Ni, P. C. Canfield, and D. R. Sánchez, *J. Phys.: Cond. Matter* **23**, 145701 (2011).
- [20] M. Sonobe and K. Asai, *J. Phys. Soc. Jpn.* **61**, 4193 (1992).
- [21] A. Abragam, *The Principles of Nuclear Magnetism*, The International Series of Monographs on Physics (Clarendon Press, Oxford, 1986).
- [22] M. M. Hrovat, P. Jeglič, M. Klanjšek, T. Hatakeda, T. Noji, Y. Tanabe, T. Urata, K. K. Huynh, Y. Koike, K. Tanigaki, and D. Arčon, *Phys. Rev. B* **92**, 094513 (2015).
- [23] R. E. Walstedt, R. Dupree, J. P. Remeika, and A. Rodriguez, *Phys. Rev. B* **15**, 3442 (1977).
- [24] P. Carretta, M. Corti, and A. Rigamonti, *Phys. Rev. B* **48**, 3433 (1993).
- [25] L. de' Medici, S. R. Hassan, M. Capone, and X. Dai, *Phys. Rev. Lett.* **102**, 126401 (2009).
- [26] D. Belitz and T. R. Kirkpatrick, *Rev. Mod. Phys.* **66**, 261 (1994).
- [27] B. L. Altshuler, D. Khmel'nitzkii, A. I. Larkin, and P. A. Lee, *Phys. Rev. B* **22**, 5142 (1980).
- [28] H. Fukuyama, *J. Phys. Soc. Jpn.* **48**, 2169 (1980).